# Transformer spin-triplet superconductivity at the onset of isospin order in bilayer graphene

Zhiyu Dong [1] Andrey V. Chubukov [2] and Leonid Levitov [1]

[1]*Department of Physics, Massachusetts Institute of Technology, Cambridge, Massachusetts 02139, USA*
[2]*W. I. Fine Theoretical Physics Institute, University of Minnesota, Minneapolis, Minnesota 55455, USA*

We consider the origin of superconductivity found recently in Bernal bilayer graphene at the onset of isospin-polarized order, trying to infer the pairing mechanism and superconducting order from the measurements available to date. The superconductivity is induced by a parallel magnetic field and persists well above the Pauli limit, indicating an unconventional scenario of quantum-critical pairing, where soft fluctuations of isospin give rise to spin-triplet superconductivity. We consider the scenario in which the pairing interaction is entirely repulsive, which stands in contrast to the typical quantum-critical pairing mechanisms. Superconductivity emerges through a "transformer" mechanism where, in the presence of an in-plane magnetic field, the incipient valley polarization converts a frequency-independent repulsion into one with a strong nonmonotonic frequency dependence. Such an interaction enables a nonzero solution for the pairing gap function that changes sign as a function of frequency. The same mechanism holds at zero field in the presence of spin-orbit coupling, providing a likely explanation for the recently observed superconductivity in bilayer graphene on the $WSe_2$ monolayer.

## I. INTRODUCTION

The quest for unconventional superconductivity (SC) governed by Coulomb repulsion rather than phonon attraction gained new momentum with the advent of graphene-based SC. In the SC phases found initially in moiré graphene [1–7], a flat-band system hosting strongly interacting electrons [8], delineating these mechanisms has proven to be a challenging task [9]. In some experiments, the SC appears to be clearly associated with correlated orders [6,7,10], suggesting nonphononic pairing scenarios [11–14]. Yet, other experiments report on SC that can be isolated (and thus decoupled) from other ordered phases [4,15], supporting phonon mechanism [16–18]. So far, no consistent picture has emerged, and presently, there is no clear verdict on the pairing mechanism. System complexity, such as the peculiar form of moiré flatband electron wave function [8,19] and multiple kinds of moiré-related disorder, in particular the twist-angle disorder, strain, and buckling, make this debate difficult to settle.

Fortunately, recent research has uncovered two non-moiré systems that exhibit intertwined superconducting orders and correlated electronic orders—the field-biased Bernal bilayer graphene [20,21] (BBG) and rhombohedral trilayer graphene [22,23] (RTG). These systems present distinct benefits for studying strongly-correlated physics owing to the simplicity of their band structure and exceptional cleanness due to the absence of strain. It is noteworthy that superconducting phases are observed in both BBG and RTG systems in close proximity to interfaces between phases with different isospin polarization. The superconducting phases track these interfaces when the system parameters are being varied, see Fig. 1.

Given these findings, it is almost inevitable to conclude that this behavior indicates presence of a pairing glue that is being mediated by a soft mode directly associated with isospin ordering. Interestingly, as discussed below, this pairing

mechanism yields a superconducting phase near the onset of isospin polarization and general properties that closely match the observations. In particular, superconductivity appears at a finite in-plane magnetic field $B_\parallel$ and survives well beyond the Pauli limit, in agreement with the experiment. The superconductivity is spin-triplet, induced by a $B_\parallel$ that creates spin imbalance as shown in Fig. 1(b) insets. Another interesting property that follows from this analysis is that, perhaps somewhat unexpectedly, the minority-spin carriers (spin-down in Fig. 1) dominate pairing, whereas the contribution of the majority-spin carriers, despite a higher density, is negligible.

We stress that this pairing scenario is distinct from the existing mechanisms of pairing mediated by critical modes [24–31]. In previously studied instances of pairing near a quantum-critical point, soft quantum-critical modes associated primarily with spin fluctuations [32] generated an effective e-e attraction by exchange-type scattering of Cooper pairs either between different Fermi surfaces [33,34] or between different hotspots on a single Fermi surface [35]. In graphene, to the contrary, the exchange component of (antisymmetrized) Coulomb interaction arising due to intervalley e-e scattering is weakened because the Fermi surface size in each valley is much smaller than the momentum transfer $\boldsymbol{K} - \boldsymbol{K}'$ for such e-e scattering processes. This renders pair scattering approximately valley-conserving, weakening the attractive exchange-type pairing interaction [36]. Likewise, the pair hopping interaction, known to be relevant for pairing in Fe-based materials, is absent in our case because in BBG the low-energy fermions are located near Dirac points $\boldsymbol{K}$ and $\boldsymbol{K}'$, but $2(\boldsymbol{K} - \boldsymbol{K}')$ is not a reciprocal lattice vector. As a result, the soft-mode-mediated pairing interaction, while being strong, is repulsive rather than attractive. Therefore understanding this unusual superconductivity requires a mechanism that converts a strong repulsion mediated by the soft modes into an attraction.

Another clue comes from the observed unique dependence of $T_c$ on a magnetic field $B_\parallel$: unlike textbook SC which is
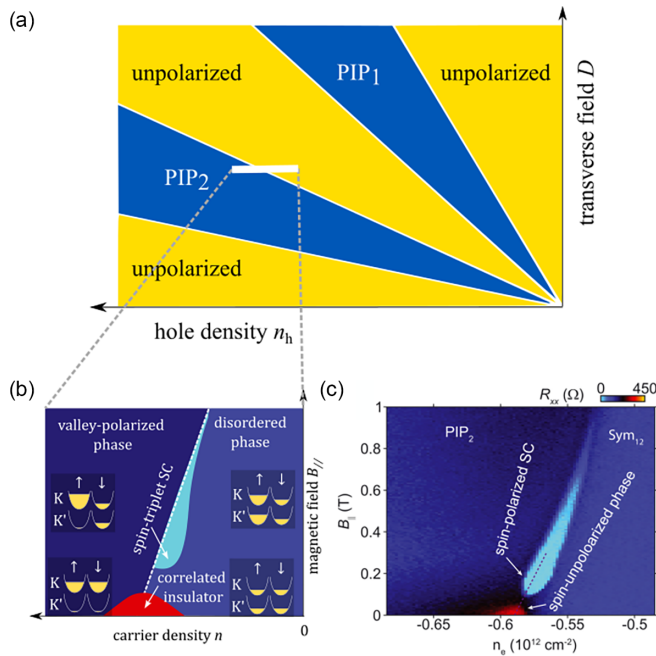
FIG. 1. (a) Phase diagram schematic for isospin orders in BBG following Ref. [20]. In phases $PIP_1$ and $PIP_2$ only one and two isospin-polarized subbands are populated, respectively. Labels indicate isospin polarization in each phase at $B_\parallel = 0$. (b) Predicted phase diagram for superconductivity governed by critical mode at the phase boundary between isospin-valley-polarized and unpolarized phases. Here ↑ and ↓ label spin-up (majority) and spin-down (minority) subbands, respectively. (c) The measured phase diagram [20] strongly resembles the phase diagram predicted in (b) [see text].

suppressed by a magnetic field, here SC is induced by $B_\parallel$ field. A finite threshold in $B_\parallel$ above which SC is observed [see Fig. 1(c)] suggests a pairing mechanism different from those studied in moiré [11–14] and RTG systems [22,37,38]. Since $B_\parallel$ only couples to spin when applied in-plane, the $B_\parallel$-induced SC indicates that spin imbalance is essential for pairing. Moreover, SC is found to persist in a high field, surviving well above the Pauli limit. The resilience of SC in a $B_\parallel$ field unambiguously points to a spin-triplet pairing and thus an unconventional pairing mechanism.

Here we demonstrate that superconducting pairing can be achieved through an attraction-from-repulsion scenario that ties together these key factors: a soft mode, repulsive Coulomb coupling, broken spin degeneracy, and pairing in the spin-triplet channel. The predictions of this scenario are in agreement with the observations [20]. In essence, at a finite $B_\parallel$, the pairing interaction, while remaining repulsive at all bosonic frequencies $\nu$, becomes strongly retarded, thereby helping an effective attraction to emerge from bare repulsion. Namely, the pairing interaction acquires a nonmonotonic frequency dependence for minority-spin carriers due to field-induced suppression of the pairing interaction at small $\nu$. We show that this suppression is "universal," meaning it is not affected by the band structure, and enables the emergence of a superconducting state with a dispersive gap that changes sign as a function of frequency. The superconducting order parameter is of a spin-triplet and valley-singlet character, featuring an $s$-wave momentum dependence. The predicted critical temperature sharply peaks near the isospin polarization threshold. Similar scenarios for conventional $s$-wave pairing in the presence of strong repulsive Coulomb repulsion have been discussed repeatedly in the literature both early on [39–42] and recently [43–45].

We also investigate an alternative, yet closely associated, pairing mechanism, which involves majority-spin electrons subject to a finite $B_\parallel$. In this scenario, the pairing interaction between majority-spin electrons, governed by the soft mode, acquires a dependence on the soft-mode momentum arising due to the $2k_F$ singularity in polarization function. Under a parallel magnetic field the $2k_F$ values for the spin-up and spin-down Fermi seas become unequal and, as a result, the pairing interaction for the majority-spin Fermi sea is modulated by the strength of the $B_\parallel$ field. This interaction induces an attraction in non-$s$-wave channels via the Kohn-Luttinger (KL) mechanism [46]. As a result, we obtain pairing in a spin- and valley-triplet, $p$-wave channel.

Pairing in either the minority-spin or majority-spin channel accounts for all the salient features observed in the experimentally determined phase diagram in BBG [see Fig. 1(c)]: First, superconductivity occurring at a phase boundary is natural for a scenario that relies on critical isospin modes. Second, the predicted superconductivity has a threshold in $B_\parallel$ field as a finite $B_\parallel$ is required to overcome bare repulsion. At a lower $B_\parallel$, we predict a strong repulsive interaction. This interaction is expected to produce a correlated insulator state, in line with the observations [Fig. 1(c)].

Further support for this mechanism comes from a recent experiment [21] that reports the observation of superconductivity in a BBG placed on top of a monolayer of $WSe_2$. In this system, superconductivity arises even when the magnetic field strength $B_\parallel$ is zero, and persists even when $B_\parallel$ values exceed the Pauli limit. This behavior can be explained within the same framework as described above by considering the influence of interfacial spin-orbit coupling (SOC) induced in graphene due to the presence of $WSe_2$. Such SOC effectively induces a valley-odd Zeeman field, which acts for SC in the same way as the magnetic field $B_\parallel$. Naturally, at a finite $B_\parallel$ the actual and effective $B$ fields combine to induce SC above the Pauli limit. Further details of this scenario are discussed in Sec. VIII.

We want to stress that the scenario we focus on below is just one of the possible mechanisms for superconductivity in BBG. Our analysis is based on two key assumptions inferred from measurements [20]. One is that the isospin order is of a valley imbalance type. The other is that superconductivity is driven by fluctuations of the $\tau_3$ valley-imbalance order parameter. Valley polarization is inferred by measuring quantum oscillation frequency and observing Fermi surface doubling in the ordered state. The absence of spin polarization is inferred from the dependence of the phase boundary on the in-plane magnetic field. As discussed in Sec. IX, this picture is in good agreement with our scenario. As for the second assumption, inferring the pairing mechanism from measurements is a difficult task. In the absence of a direct experimental input, one is led to proceed by trial and error by relying on circumstantial evidence.

There are several possible pairing mechanisms that could be viable candidates for superconductivity in BBG. One such

mechanism is related to superconductivity recently explored in RTG, namely pairing mediated by inter-valley-coherence (IVC) soft modes [47,48]. Even if, following the first assumption, the PIP$_2$ phase is identified with valley-imbalanced order, there are still several types of soft modes that can drive pairing. In particular, the collective mode in IVC channel can produce a significant pairing interaction, given that the BBG system has an approximate SU(4) spin-valley symmetry. This makes IVC soft mode a credible candidate for the pairing glue. This scenario is supported by recent work that links certain unique features in the measured SC phase diagrams to the IVC picture [48].

These alternative possibilities notwithstanding, here we will focus on the pairing induced by the valley-imbalance soft mode as the most straightforward and logical mechanism. Interestingly, besides predicting the spin-triplet pairing suggested by measurements, this mechanism can account for the unusual magnetic field dependence of the observed superconductivity that emerges when the magnetic field surpasses a certain threshold. This peculiar behavior cannot be easily explained by other mechanisms, but it finds a natural and compelling explanation within the framework proposed below.

## II. PAIRING NEAR THE ONSET OF VALLEY POLARIZATION

Motivated by the observed relation between valley polarization instability and the emergence of superconductivity, here we employ a minimal model for the former and discuss its implications for the latter. We consider susceptibilities for the valley and spin imbalances, the quantities that diverge near the onset of valley or spin polarization. These quantities can be linked to the free-fermion density-density response function in a standard manner. With this framework established, we are able to investigate the "transformer" pairing glue that emerges at the onset of instability, and analyze its distinctive characteristics and the properties of the resulting superconducting state.

First, we describe the hierarchy of energy scales in our problem. In the regime where superconductivity occurs, the bandgap created by the displacement field is approximately 100 meV [20]. Band-structure calculations [49,50] predict a Fermi energy of roughly 10 meV at the carrier density and $D$ field values where superconductivity occurs. This Fermi energy is much smaller than the bandgap of $D$. The electron-electron interaction energy is expected to be comparable to the Fermi energy, as the system is close to an isospin Stoner instability. The experiment reports a relatively small superconducting transition temperature ($T_c$) of 30 mK, which is comparable to the minimal Zeeman energy $\approx 1 \times 10^{-2}$ meV required to create superconductivity upon increasing $B_\parallel$ [20]. Since this value is much smaller than the interaction and kinetic energies, we will ignore the Zeeman energy at first and account for it perturbatively later.

We model the interacting electrons in BBG using a short-range interaction

$$H = \sum_i \epsilon_i(\boldsymbol{p})\psi_{i\boldsymbol{p}}^\dagger \psi_{i\boldsymbol{p}} + \sum_{ii'} \frac{V_0}{2} \psi_{i\boldsymbol{p}+\boldsymbol{q}}^\dagger \psi_{i'\boldsymbol{p}'-\boldsymbol{q}}^\dagger \psi_{i'\boldsymbol{p}'} \psi_{i\boldsymbol{p}}, \quad (1)$$

where $i, i' = K\uparrow, K\downarrow, K'\uparrow, K'\downarrow$ are isospin indices. A single-band model $\epsilon_i(\boldsymbol{p})$ will be used as a proxy for a more realistic Dirac band. This single-band model Eq. (1) is obtained by projecting the two-band model of BBG [49,50] on the conduction band, which in the regime of $D \gg E_F$ is well isolated from the valence band. This band projection in general yields wavefunction formfactors $\langle u_p | u_{p+q} \rangle$, where $|u_p\rangle$ is the cell-periodic part of the Bloch function. In Eq. (1), we take the form factors to be unity, as appropriate for the case $D \gg E_F$ [51]. Indeed, for the states obtained from a simple two-band Hamiltonian [49,50] the form factors at small energies $E_F \ll D$ are close to unity, with the deviation being as small as $E_F/D$. Therefore Eq. (1) provides a reasonable approximation so long as $D \gg E_F$, regardless of the band-structure details such as the trigonal warping [49,50].

In Eq. (1), the momentum-independent electron-electron interaction $V_0$ represents a repulsion short-ranged as compared to Fermi wavelength. This interaction mimics Coulomb $1/r$ interaction screened out at momentum transfers smaller than $2k_F$, taken here as an estimate for the screening parameter in the Thomas-Fermi model. Equation (1) only accounts for the intravalley scattering processes. The intervalley carrier scattering processes mediated by the $1/r$ interaction can be ignored because the $1/r$ interaction form factor drops rapidly for momentum transfers $2k_F < q < q_{max} \sim |\boldsymbol{K} - \boldsymbol{K}'|$, where the ratio $q_{max}/2k_F$ can be as large as a 100 for BBG.

In the graphene bilayer, an isospin polarization in the valley ($\tau$) and spin ($\sigma$) subspaces can conceivably occur through various routes, with the main scenarios being the following.

(1) A $q = 0$ instability towards valley-only polarization ($M = \tau_3, \sigma_0$).

(2) A $q = 0$ instability towards intravalley ferromagnetism (FM) ($M = \tau_0 \pm \tau_3, \sigma_n$).

(3) An instability with momenta $\boldsymbol{K} - \boldsymbol{K}'$ in either charge channel ($\tau_\pm, \sigma_0$) or spin channel ($M = \tau_\pm, \sigma_n$) (see, e.g., Refs. [52,53]).

Matrices $M$ in spin/valley space describe the orders through a spontaneously generated fictitious field term in the Hamiltonian,

$$\delta H = \sum_{\boldsymbol{p}i} \psi_{i\boldsymbol{p}}^\dagger M_{ii'} \psi_{i'\boldsymbol{p}}, \quad (2)$$

where $i, i'$ label spin and valley degrees of freedom. Here $\tau_m$ and $\sigma_n$ ($m, n = 0, 1, 2, 3$) are valley and spin Pauli matrices, and $\sigma_0$ is the identity $2 \times 2$ spin matrix. In our simplified model, we find that these instabilities are degenerate. However, in a more realistic scenario involving a generic interaction, one of the instabilities will typically dominate and lift the degeneracy, as discussed below.

Needless to say, presently our understanding of the system is far from complete. Experiments identified the ordered phase PIP$_2$ as a valley-polarized phase [20]. The method used relied on measuring quantum oscillations in an out-of-plane field, combined with the measurements of the phase diagram in an in-plane field. Ref. [20] concludes that the ordered state is valley-polarized and spin unpolarized, yet the existing data do not allow to distinguish between different valley polarization orders such as valley imbalance and inter-valley coherence. Acknowledging that the specific type of polarization remains
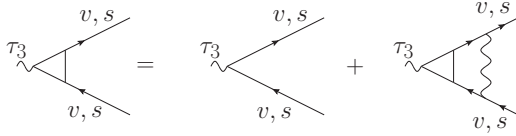
FIG. 2. Ladder diagrams describing the valley-polarization instability in a mean-field approximation. Here $v$ and $s$ are valley and spin indices $K$, $K'$ and $\uparrow$, $\downarrow$ The lines with arrows represent Green's functions, the wavy line is the electron-electron interaction, vertices represent the $\tau_3$ Pauli matrix in valley subspace. No summation over $v$ and $s$ is assumed.

unknown, here we proceed with the scenario in which this phase features a valley imbalance order.

An instability towards valley polarization, described by the $M = \tau_3$ matrix, can be represented diagrammatically, as shown in Fig. 2, where arrows represent the electron Green's functions $G_s(\omega, \boldsymbol{p}) = 1/(i\omega - \epsilon_s(\boldsymbol{p}))$ and the wave lines represent the interaction. Summing up ladder diagrams in the $\tau_3$ channel yields a standard Stoner-like condition for the instability threshold (see, e.g., Ref. [52]):

$$V_0 \Pi_{3,s} = -1, \quad \Pi_{3,s} = \frac{1}{2} \sum_{\omega, \boldsymbol{p}} \text{tr}(\tau_3 \mathcal{G}_s(\omega, \boldsymbol{p}) \tau_3 \mathcal{G}_s(\omega, \boldsymbol{p})). \tag{3}$$

where the quantity $\Pi_{3,s}$ denotes the polarization in the valley channel. Here $s = \uparrow, \downarrow$ denotes electron spin, tr is a valley trace involving summation over valley indices, with the spin indices not being summed over. The quantities $\mathcal{G}_s(\omega, \boldsymbol{p})$ are Green's functions of spin-$s$ electrons, each being a $2 \times 2$ matrix in valley space:

$$\mathcal{G}_s(\omega, \boldsymbol{p}) = \begin{pmatrix} G_{Ks}(\omega, \boldsymbol{p}) & 0 \\ 0 & G_{K's}(\omega, \boldsymbol{p}) \end{pmatrix}. \tag{4}$$

In our notations, $\Pi_{3,s}$ is negative, so the instability develops at a positive $V_0$. The corresponding valley-polarization susceptibility is

$$\chi_{v,s} = \frac{\Pi_{3,s}}{1 + V_0 \Pi_{3,s}}, \tag{5}$$

where the subscript $v$ stands for valley polarization. It follows directly from Eq. (3) that the free-fermion polarization functions obey

$$\Pi_{3,s} = \Pi_s^K = \Pi_s^{K'}, \tag{6}$$

where $\Pi_s^v = \sum_{\omega, p} G_{vs}(\omega, p) G_{vs}(\omega, p)$, $v = K$, $K'$ is the bare polarization bubble (bare susceptibility) in valleys $K$ and $K'$. The identity $\Pi_s^K = \Pi_s^{K'}$ follows from the mirror symmetry that maps valleys $K$ and $K'$ on each other. Due to this symmetry, the free-fermion dispersion behaves as $\epsilon(K + \boldsymbol{p}) = \epsilon(K' - \boldsymbol{p})$, and, therefore, $\Pi_s^K = \Pi_s^{K'}$. Below we suppress the valley index, i.e., replace $\Pi_s^K$ and $\Pi_s^{K'}$ by just $\Pi_s$. For free electrons with parabolic dispersion and at a zero magnetic field, $\Pi_s = -\nu$, where $\nu$ is the density of states at $\epsilon = \epsilon_F$ for one isospin species.

We emphasize that while the valley susceptibility diverges, the ordinary charge susceptibility $\chi_{c,s}$, obtained by the ladder

summation similar to that in Fig. 2, but with $\tau_3$ replaced with an identity matrix and the interaction being a sum of the Hartree and Fock contributions, shows no divergence. Explicit calculation yields

$$\chi_{c,s} = \frac{\Pi_s}{1 + V_0 \Pi_s - 2 \sum_{s'} V_0 \Pi_{s'}}. \tag{7}$$

The factor of 2 before the summation over spin $s'$ is due to the twofold valley degeneracy [see Eq. (6)]. At zero magnetic field, where $\Pi_s = \Pi$, this reduces to

$$\chi_{c,s} = \frac{\Pi}{1 - 3V_0 \Pi}, \tag{8}$$

where the factor $3 = 4 - 1$ arises as a combination of the Hartree and Fock terms in Eq. (7). The Hartree term is four times greater than the Fock term and is of the opposite sign, which suppresses the charge instability.

At a nonzero magnetic field, the values $\Pi_\uparrow$ and $\Pi_\downarrow$ are different, and the analysis requires more care. Performing the same computation as above and noting that, in the calculation, the $\uparrow$ and $\downarrow$ spin components decouple, and Eq. (5) holds. Then valley instability for spin $\uparrow$ occurs at $V_0 \Pi_\uparrow = -1$, whereas for spin $\downarrow$ it occurs at $V_0 \Pi_\downarrow = -1$. In experiment [20], valley polarization is pushed to a lower density at an increasing $B_\parallel$ field [see Fig. 1(c)]. Comparing this to the Stoner instability picture indicates that criticality in a finite $B_\parallel$ is linked to the majority-spin carriers. In our model, this implies that $|\Pi_\uparrow| > |\Pi_\downarrow|$, and the leading instability occurs at $V_0 \Pi_\uparrow = -1$.

With the valley polarization instability framework established, we proceed to discuss how the attraction-from-repulsion pairing mechanism arises at the onset of valley polarization. It is instructive to outline the physics of this mechanism before proceeding with calculations. In the presence of a magnetic field, valley polarization first emerges for spin-up (majority-spin) carriers. This makes spin-up valley-polarizing excitations gapless, whereas excitations in spin-down (minority-spin) Fermi seas remain gapped. Softening of valley-polarizing modes leads to a vanishing of $1 + V_0 \Pi_\uparrow$, while $1 + V_0 \Pi_\downarrow$ remains finite. These two combinations appear in equal-spin pairing vertices $\Gamma_{s,s}$ as $\Gamma_{\uparrow,\uparrow} \propto 1/(1 + V_0 \Pi_\uparrow)$ and $\Gamma_{\downarrow,\downarrow} \propto (1 + V_0 \Pi_\uparrow)/(1 + V_0 \Pi_\downarrow)^2$.

These quantities, which describe superconductivity in the spin-up and spin-down channels, have a very different behavior at the valley polarization instability. The pairing vertex for spin-up carriers, $\Gamma_{\uparrow,\uparrow}$, diverges at the transition. However, it is of a repulsive sign and monotonically decreases with frequency. For such a vertex, the superconductivity selfconsistency equation has no nonzero solution for the gap function. However, the quantity $\Gamma_{\downarrow,\downarrow}$ shows a different behavior because of the factor $1 + V_0 \Pi_\uparrow$ that vanishes near the instability. This gives a negative feedback effect on $\Gamma_{\downarrow,\downarrow}$ and, as a result, this quantity is substantially reduced at small frequencies. The frequency dependence of $\Gamma_{\downarrow,\downarrow}$ then becomes nonmonotonic, dropping from more repulsive at high frequencies to less repulsive at low frequencies. This frequency dependence, despite the positive sign of $\Gamma_{\downarrow,\downarrow}$, allows spin-down electrons to form spin-triplet Cooper pairs with a sign-changing gap function $\Delta(\omega)$.
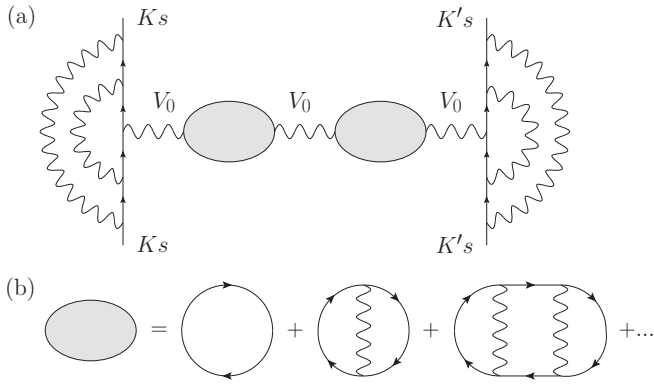
FIG. 3. (a) Diagrams describing the effective pairing interaction between electrons in valleys $K$ and $K'$ mediated by quantum-critical modes, Eq. (11). These processes give an enhancement to forward scattering divergent near the valley-polarization instability (see text). (b)The diagrammatic representation of the irreducible part of the charge susceptibility $\chi_{c,s}$ (the shaded ellipse), summed over $s = \uparrow, \downarrow$.

Below we first discuss the pairing interaction at a zero magnetic field $B_\parallel = 0$, where $\Pi_{s=\uparrow} = \Pi_{s=\downarrow} = \Pi$ (see Sec. III), and then extend the results to finite $B_\parallel$, where $\Pi_{s=\uparrow} \neq \Pi_{s=\downarrow}$ and the frequency dependence of the pairing interaction becomes nonmonotonic, leading to superconductivity (see Sec. IV).

## III. REPULSION AT $B_\parallel = 0$

It is instructive to begin with $B_\parallel = 0$. In this case, the pairing interaction is repulsive and has a monotonic frequency dependence. This behavior, which is incompatible with pairing, will be contrasted in Sec. IV with that arising at a finite $B_\parallel$, where the interaction remains repulsive but acquires a nonmonotonic frequency dependence that leads to pairing.

We start by noting that the pairing interaction with zero total momentum occurs between fermions in different valleys, $K$ and $K'$. At the lowest order, the pairing interaction is just $V_0$, however near the onset of the valley polarization order dressing the interaction with soft modes becomes essential. We argue below that the relevant dressing is the one illustrated in Fig. 3. The property of this dressing that will be important for us is that it enhances the pairing interaction by a large factor $1/(1 + V_0\Pi)$. We proceed by analyzing how these diagrammatic series shown in Fig. 3 emerge in order-by-order expansion in $V_0$.

To describe the pairing, we consider the irreducible vertex function in the pairing channel, $\Gamma_{ss'}$, where $s$ and $s'$ denote spin components. By general rules, $\Gamma_{ss'}$ is a fully dressed antisymmetrized interaction describing scattering between fermion pair states $(\boldsymbol{k}, -\boldsymbol{k}) \to (\boldsymbol{p}, -\boldsymbol{p})$. The specifics of our case are that (i) pairing involves one fermion near $K$ and one near $K'$, and (ii) the scattering between $K$ and $K'$ is weak in graphene and can be neglected. In this situation, the contributions to $\Gamma_{ss}$ from antisymmetrization vanish, $\Gamma_{s,s'}$ becomes spin-independent $\Gamma_{s,s'} = \Gamma$ and we only need to analyze how the direct pairing interaction $V_0$ is being dressed.

To second order in $V_0$, we have three topologically distinct diagrams shown in Fig. 4. The first two diagrams [see panels
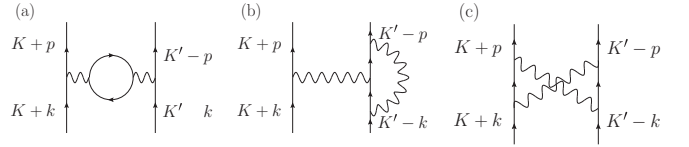


FIG. 4. Three types of second-order diagrams: (a) bubble diagram; (b) "wine glass" diagram; and (c) "exchange" diagram.

(a) and (b)] are known as bubble and "wine glass" diagrams. Since the two intermediate electron lines in each of these two diagrams are from the same valley, their contributions are the same as from irreducible processes in Fig. 2—the ones which give rise to valley polarization. In comparison, the last diagram, known as the "exchange" diagram, contains two intermediate electron lines in which one is from valley $K$, whereas the other is from valley $K'$ [see panel (c)]. Its contribution is not directly related to the processes leading to valley polarization. Because our goal is to analyze how the pairing interaction evolves near the onset of valley polarization, we focus on the diagrams with a leading-order divergence. We, therefore, neglect the "exchange" diagrams at each order of expansion in $V_0$ and include only the bubble and "wine glass" diagrams (see Ref. [54] for similar consideration). Some examples of the leading-order diagrams at a three-loop order are shown in Fig. 5(a). These are diagrams with zero, one, and two bubbles. In comparison, several typical subleading diagrams at a 3-loop order are shown in Fig. 5(b).

The sum of the bubble and wine glass diagrams can be rewritten as illustrated in Fig. 3. Below, we work out the analytical expression. First, diagrams without bubbles sum up into $V_0\gamma^2$, where

$$\gamma = \frac{1}{1 + V_0\Pi}. \tag{9}$$

We next account for the polarization bubbles. Insertion of one bare bubble contributes the factor $-4V_0\Pi$, where $-1$ is
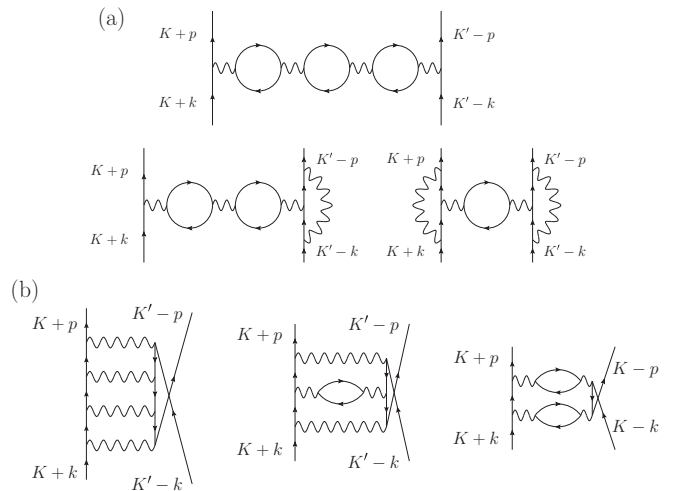


FIG. 5. Diagrams at three-loop order: (a) diagrams with 3 bubbles that are maximally divergent near the Stoner instability and (b) diagrams with 0, 1, and 2 bubbles, which are subleading at the Stoner instability.

due to a fermionic loop and the factor of 4 arises due to spin and valley degeneracy. An insertion of ladder series of interactions into each bubble further converts $\Pi$ into fully dressed irreducible $\Pi\gamma$. The resulting effective interaction described by these diagrams can thus be written as

$$\Gamma = \gamma^2 \frac{V_0}{1 - 4V_0\Pi\gamma} \tag{10}$$

$$= \frac{V_0}{(1 + V_0\Pi)(1 - 3V_0\Pi)}. \tag{11}$$

This vertex function contains the factor $1/(1 + V_0\Pi)$ and hence it gets enhanced near the onset of valley polarization. Near $V_0\Pi = -1$, it can be approximated as

$$\Gamma \approx \frac{V_0}{4} \frac{1}{1 + V_0\Pi}. \tag{12}$$

Still, the interaction remains positive-valued, i.e., repulsive. This behavior is distinct from that found for pairing mediated by a critical $q = 0$ mode in other systems, such as a nematic QCP [24–26]. Indeed, in these systems electrons with **k** and $-$**k** live on the same Fermi surface and interact through exchange processes. In our case, such a process is forbidden as it requires a fermion to scatter from one valley to the other.

For a more accurate treatment, we should take into consideration the fact that the valley polarization instability is the one with zero momentum transfer ($q = 0$) and zero frequency transfer ($\nu = 0$). At a finite $q$ and a finite $\nu$, the polarization $\Pi$ becomes the function of both, $\Pi = \Pi(\nu, q)$, and the vertex $\Gamma$ also becomes $\Gamma(\nu, q)$. The static polarization bubble is a regular function of $q^2$ and the dominant contribution to the dynamical part comes from the Landau damping (see, e.g., Ref. [42]). Then

$$1 + V_0\Pi(\nu, q) \approx \frac{|\nu|}{v_F q} + Kq^2 + \delta, \tag{13}$$

where $\delta = 1 + V_0\Pi(0, 0)$ characterizes a detuning from the valley-polarization phase boundary. The stiffness parameter $K$ and the Fermi velocity $v_F$ are determined by band dispersion $\epsilon(p)$. In writing the Landau damping term, we assumed that $|\nu| \ll v_F q$. Plugging this $\Pi(\nu, q)$ into Eq. (12), we obtain the vertex $\Gamma(\nu, q)$ at small $q$ and $\nu$ in the form

$$\Gamma(\nu, q) = \frac{V_0}{4} \frac{1}{\frac{|\nu|}{v_F q} + Kq^2 + \delta}. \tag{14}$$

This effective interaction with the dynamical Landau-damping term is similar to the one studied in the context of quantum-critical pairing in metals on the verge of an Ising-nematic or Ising-ferromagnetic instability [28,30,55] and for 2D fermions coupled to emerging gauge field in a doped Mott insulator [56–60]. However, the sign of the interaction in our case is repulsive, and it monotonically decreases with frequency. Such an interaction does not lead to superconductivity.

## IV. ATTRACTION FROM REPULSION AT $B_\parallel \neq 0$

Here we consider how the pairing interaction, Eq. (14), is altered at $B_\parallel \neq 0$. We show that, while it remains repulsive, it becomes nonmonotonic in frequency for fermions with

spin direction opposite to the field. This leads to pairing for minority-spin carriers, as we demonstrate.

At a finite $B_\parallel$, the polarization bubble $\Pi_s$ does depend on spin $s = \uparrow, \downarrow$ and this has to be included in the calculation of the pairing vertex $\Gamma_{s,s'}$. We will focus on equal-spin channel $s = s'$. Repeating the same calculations as above, but keeping the dependence on $s$ in $\Pi_s$, we obtain

$$\Gamma_{s,s} = V_0\gamma_s^2 \frac{1}{1 - 2V_0 \sum_{s'} \Pi_{s'}\gamma_{s'}}, \tag{15}$$

where $\gamma_s = 1/(1 + V_0\Pi_s)$. This can be re-expressed as

$$\Gamma_{s,s} = \frac{(1 + V_0\Pi_\uparrow)(1 + V_0\Pi_\downarrow)V_0}{(1 + V_0\Pi_s)^2 \left[ 1 - V_0(\Pi_\uparrow + \Pi_\downarrow) - 3V_0^2\Pi_\uparrow\Pi_\downarrow \right]}. \tag{16}$$

As before, each polarization bubble is a function of $\nu$ and **s**, such that

$$1 + V_0\Pi_s(\nu, q) \approx \frac{|\nu|}{v_F q} + Kq^2 + \delta_s, \tag{17}$$

Here and below, for simplicity, we take the Fermi velocities and the stiffness parameters for both spin species to be equal, $v_{F,\uparrow} = v_{F,\downarrow} = v_F$, $K_\uparrow = K_\downarrow = K$. The quantities $\delta_{s=\uparrow,\downarrow}$, which define the detuning from the phase boundary, are equal in the absence of $B_\parallel$-induced Zeeman interaction but become unequal when $B_\parallel \neq 0$. Comparing the two denominators in Eq. (16), we find that the leading instability in a magnetic field occurs at either $V_0\Pi_\uparrow = -1$ or $V_0\Pi_\downarrow = -1$. As discussed in Sec. II, experiments indicate [20] that criticality at a finite $B_\parallel$ occurs first for majority-spin carriers. This translates into $\delta_\uparrow = 0$ at the onset of valley polarization, whereas $\delta_\downarrow$ remains finite. As a result, $V_0\Pi_\uparrow \approx -1$, and in the right-hand side of Eq. (16), $1 - V_0(\Pi_\uparrow + \Pi_\downarrow) - 3V_0^2\Pi_\uparrow\Pi_\downarrow \approx 2(1 + V_0\Pi_\downarrow)$. As a result,

$$\Gamma_{\uparrow,\uparrow} \approx \frac{V_0}{2} \frac{1}{1 + V_0\Pi_\uparrow} = \frac{V_0}{2} \frac{1}{\frac{|\nu|}{v_F q} + Kq^2 + \delta_\uparrow} \tag{18}$$

and

$$\Gamma_{\downarrow,\downarrow} \approx \frac{V_0}{2} \frac{1 + V_0\Pi_\uparrow}{(1 + V_0\Pi_\downarrow)^2} = \frac{V_0}{2} \frac{\frac{|\nu|}{v_F q} + Kq^2 + \delta_\uparrow}{\left(\frac{|\nu|}{v_F q} + Kq^2 + \delta_\downarrow\right)^2}. \tag{19}$$

Both vertices remain positive (repulsive), but they now have qualitatively different frequency dependence: $\Gamma_{\uparrow\uparrow}$ is similar to that found for $B_\parallel = 0$, and is monotonically decreasing with $\nu$. On the contrary, the pairing interaction for minority-spin electrons $\Gamma_{\downarrow\downarrow}(\nu, q)$ has a nonmonotonic frequency dependence because at small momentum $q \ll \sqrt{\delta/K}$, it is strongly suppressed at low frequencies $\nu < v_F|q|\delta_\downarrow$ and not suppressed at $\nu > v_F|q|\delta_\downarrow$. Then $\Gamma_{\downarrow\downarrow}$ increases at low frequencies and decreases at higher frequencies.

The $s$-wave component of this vertex (by far the largest one for small Fermi pockets, $2k_F \ll |K - K'|$) is the average of $\Gamma_{\downarrow\downarrow}(\nu, q)$ over the momentum transfers on the Fermi surface $\overline{\Gamma}_{\downarrow\downarrow}(\nu) = 2\int_0^{\sim k_F} \frac{dq}{2\pi}\Gamma_{\downarrow\downarrow}(\nu, q)$. This quantity can be cast into a scaling form

$$\overline{\Gamma}_{\downarrow\downarrow}(\nu) = \frac{V_0 k_F}{2\pi\delta_\downarrow} S(x, x_1), \quad x = \frac{\nu}{\nu_0}, \quad x_1 = \frac{\nu_1}{\nu_0}, \tag{20}$$
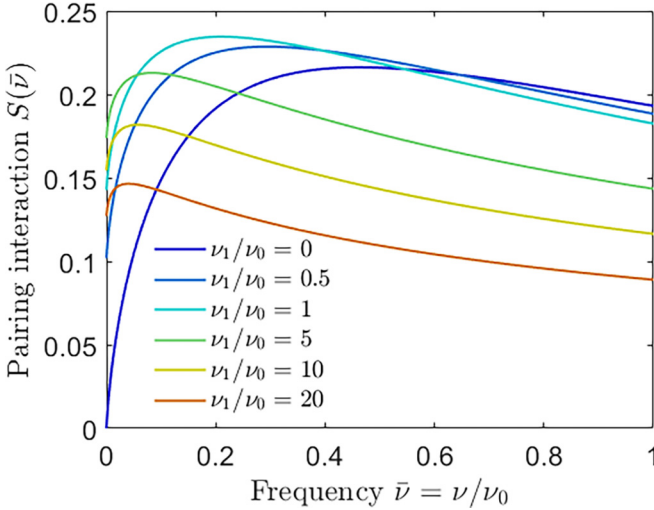
FIG. 6. Frequency-dependent pairing interaction $S(\bar{\nu})$, Eq. (23), describing the universal contribution of a soft mode. The nonmonotonic frequency dependence, which is a generic property of $S(\bar{\nu})$ for all values of the stiffness $K$, allows for a repulsive interaction to generate an attractive effective pairing interaction. The value at $\nu = 0$ is finite at $K > 0$ and zero at $K = 0$. In the latter case superconducting $T_c$ is nonzero for any $\delta_\downarrow$, the detuning from the critical point for spin-down fermions.

where $\nu_0 = E_F \delta_\downarrow$, $\nu_1 = E_F K k_F^2$, and $E_F = v_F k_F$. At $\nu_1 \ll \nu_0$, the function

$$S(x, 0) = x\left(\log\frac{1+x}{x} - \frac{1}{1+x}\right) \quad (21)$$

is manifestly nonmonotonic: it increases with $x$ at small $x$, passes through a maximum at $x \sim 0.5$, and drops at higher $x$. We emphasize that the nonmonotonic behavior is fully induced by $B_\parallel$, which splits $\delta_\uparrow$ and $\delta_\downarrow$. The nonmonotonic dependence holds if we increase the ratio $\nu_1/\nu_0$ as illustrated in Fig. 6.

Below we solve the gap equation to demonstrate that a nonmonotonic frequency dependence of $\overline{\Gamma}_{\downarrow\downarrow}(\nu)$ leads to pairing between spin-minority carriers at a nonzero $T_c$. The gap function is $s$-wave and changes sign as a function of frequency. For majority-spin carriers, the interaction is monotonic in frequency [see Eq. (18)] and does not give rise to pairing. As a result, in some range of $T < T_c$, the system simultaneously hosts both metallic carriers and superconducting pairs, unless a magnetic scattering is introduced. The coexistence of two types of carriers can be probed by searching for in-gap states in tunneling spectroscopy due to metallic carriers.

We note the decoupling between fermions with opposite spins no longer holds in a general setting. As we will see later in Sec. VI, in a generalized model, pairing susceptibilities for spin-up and spin-down fermions are coupled. In this case, the development of a superconducting gap for minority-spin carriers generates a smaller, but finite gap for majority-spin carriers. Still, tunneling experiments should reveal states with energies between smaller and larger gaps.

## V. SOLVING THE GAP EQUATION

The superconducting gap equation for the pairing of spin-down fermions, mediated by $\overline{\Gamma}_{\downarrow\downarrow}(\nu)$, is

$$\Delta(\omega) = -\frac{T_c}{2v_F}\sum_{\omega'=\pi T_c(2n+1)}\frac{\Delta(\omega')\overline{\Gamma}_{\downarrow\downarrow}(\omega-\omega')}{|\omega'|}, \quad (22)$$

The overall minus sign reflects that the interaction is repulsive. The gap equation takes a universal form when expressed in terms dimensionless $\bar{T}_c = T_c/\nu_0$ and $\bar{\omega} = \omega/\nu_0$:

$$\Delta(\bar{\omega}) = -\lambda\pi\bar{T}_c\sum_{\bar{\omega}'=\pi\bar{T}_c(2n+1)}\frac{\Delta(\bar{\omega}')}{|\bar{\omega}'|}S(\bar{\omega}-\bar{\omega}', 0), \quad (23)$$

where $\lambda = k_F V_0/(4\pi^2 v_F \delta_\downarrow)$. Because $S(\bar{\omega}-\bar{\omega}', 0)$ is strongly peaked at $|\bar{\omega}-\bar{\omega}'| = \bar{\nu}_* \approx 0.5$, one can change the overall sign in Eq. (23) by searching for gap functions which change sign under $\bar{\omega} \to \bar{\omega} + \bar{\nu}_*$. At small $\lambda$, analytical consideration yields $T_c \propto \omega_0 e^{-1/\lambda^2}$ (Ref. [44]). At $\lambda \lesssim 1$, $T_c \sim \omega_0$, but with a numerically small prefactor. At larger $\lambda$, the prefactor increases and at $\lambda \gg 1$ (i.e., at small $\delta_\downarrow$), $T_c \sim \lambda\nu_0 \sim E_F$.

For completeness, the analysis of the pairing problem at large $\lambda$ must also include fermionic self-energy. This is required because the pair-breaking effect due to self-energy may suppress superconductivity. To gain insight, one can start with the intravalley analog of the leading-order diagrams for the pairing interaction $\Gamma_{\downarrow\downarrow}(\nu, q)$ pictured in Fig. 3. Replacing fermions in different valleys with fermions in identical valleys yields a divergent contribution to the intravalley interaction, which, in turn, produces a large contribution to the self-energy. Does this imply that near Stoner instability the self-energy diverges in the same way as the pairing interaction and, through pair-breaking effects, can suppress pairing?

This concern turns out to be unfounded because, for an intravalley interaction, focusing solely on the intravalley analogs of the diagram in Fig. 3 is not justified. One must also consider other diagrams that are allowed for intravalley scattering. The contributions of these diagrams tend to suppress the divergence of the effective interaction at Stoner instability. In particular, the "exchange" processes pictured in Fig. 4(c) that were negligible for the intervalley pairing interaction (see Sec. III), can contribute to the intravalley density-density interaction and impact the self-energy. However, when these diagrams are accounted for, every time we draw a bubble, we must add to it an "exchange" contribution that looks like Fig. 4(c). These "exchange" diagrams tend to cancel the contributions from the bubbles since these two types of diagrams differ by a sign arising from a fermionic loop. As a result, the intravalley interaction that dominates the self-energy does not diverge at the Stoner instability as strongly as the pairing interaction $\Gamma_{\downarrow\downarrow}$ does.

Furthermore, in Appendix A, we analyze the impact of the self-energy on $T_c$ in a different way. We obtain the self-energy accounting only for the intravalley analog of the diagram in Fig. 3. This method, as argued above, grossly overestimates the self-energy. Nevertheless, we find $T_c$ values that are still acceptable. This observation further justifies ignoring self-energy in our analysis.
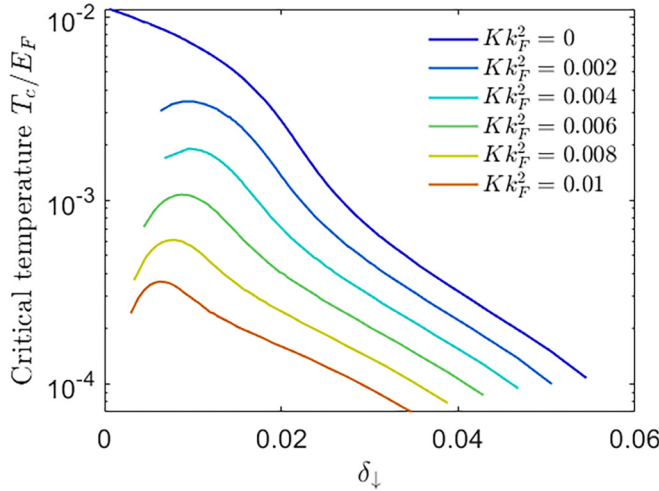
FIG. 7. Critical temperature $T_c$ vs the detuning from criticality $\delta_\downarrow$ for spin-down carriers, a parameter controlled by $B_\parallel$. For $K = 0$, $T_c$ is finite for all $\delta$. For $K \neq 0$, to the contrary, each curve starts at a finite threshold value $\delta_\downarrow > 0$. As $K$ grows, the threshold value first grows and then decreases, reflecting the behavior of $S(\nu)$ at small $\nu$ shown in Fig. 6 (see text).

Critical temperature values $T_c$, obtained by numerical solution of Eq. (23), are shown in Fig. 7. We set $k_F V_0/(2\pi v_F) = 1$, as required for a Stoner instability, and set $E_F = 10$ meV. We see that at $\nu_1 = 0$, $T_c$ monotonically increases with decreasing $\delta_\downarrow$ and at small $\delta_\downarrow$ saturates at roughly 1 K.

For a more realistic case of $\nu_0 \sim \nu_1$, the momentum-averaged $\overline{\Gamma}_{\downarrow\downarrow}(\nu)$ tends to a finite value at $\nu = 0$, leading to a smaller $T_c$ and also setting a threshold on $\delta_\downarrow$ as an $s$-wave pairing by a frequency-dependent repulsion is a threshold phenomenon [43–45], and at a small $\delta_\downarrow$ the nonmonotonicity of $\overline{\Gamma}_{\downarrow\downarrow}(\nu)$ is too weak to give rise to a pairing when the self-energy is included. At larger $\delta_\downarrow$, $T_c$ also drops because the coupling $\lambda$ gets smaller. This gives rise to a domelike dependence of $T_c$ on $\delta_\downarrow$ at a given $K k_F^2$ value. For $K k_F^2 = 10^{-2}$, we obtained at $T_c \sim 35$ mK at optimal $\delta_\downarrow = 7 \times 10^{-3}$. This value is in line with experimental $T_c$.

## VI. ROBUSTNESS OF THE TRANSFORMER PAIRING MECHANISM

To test the robustness of the attraction-from-repulsion pairing mechanism, here we demonstrate that the nonmonotonic frequency dependence of the pairing interaction, a property central to our pairing mechanism, is a general behavior. To this end, we analyze a generalized model where different types of isospin instabilities are nondegenerate.

As a reminder, as stated in the Introduction, the minimal model we studied above does not distinguish various types of isospin instabilities. Namely, in the model with the interactions with small momentum transfer all equal to $V_0$, the threshold for the valley polarization coincides with the Stoner threshold for intravalley ferromagnetism and with the threshold for a charge or spin order with momentum $\mathbf{K} - \mathbf{K}'$. Indeed, performing the same calculations as we did in Sec. II, for the other two instabilities, we find that all three occur at $V_0 \Pi_s = -1$. This degeneracy, however, does not hold beyond

the model with a single $V_0$ interaction. To see this, we extend the model to two types of density-density interactions: $V_0$ for the density-density coupling in the same valley, and $V_0'$ for the density-density coupling between different valleys. Evaluating the instability criteria, we find that the valley-polarization instability occurs at

$$(2V_0' - V_0)\Pi_s = -1, \quad (24)$$

while intravalley ferromagnetic (FM) instability occurs at

$$V_0 \Pi_s = -1, \quad (25)$$

and charge/spin instability with momentum $\mathbf{K} - \mathbf{K}'$ occurs at

$$V_0' \Pi_s = -1. \quad (26)$$

As a result, valley polarization is the leading instability when $V_0' > V_0$. In the opposite case $V_0 > V_0'$, the intravalley FM is the leading instability.

The analysis at a finite field is a bit involved because once $V_0' > V_0$, valley polarization instabilities for spin-up and spin-down fermions do not decouple, i.e., there is a single instability, at which both $\chi_{v,\uparrow}$ and $\chi_{v,\downarrow}$ diverge simultaneously. The instability condition is

$$1 + V_0'(\Pi_\uparrow + \Pi_\downarrow) + \Pi_\uparrow \Pi_\downarrow V_0(2V_0' - V_0) = 0. \quad (27)$$

Still, when $|\Pi_\uparrow| > |\Pi_\downarrow|$, $\chi_{v,\uparrow} > \chi_{v,\downarrow}$, and the instability predominantly involves fermions with spin up.

Below, we calculate the pairing vertex in the $V_0$-$V_0'$ model. The bare pairing vertex in this model is $V_0'$ because $\mathbf{k}$ and $\mathbf{k}'$ belong to different valleys. The fully dressed irreducible one at $B_\parallel = 0$ is

$$\Gamma = \frac{V_0'}{(1 - V_0 \Pi)^2 - (2V_0' \Pi)^2}. \quad (28)$$

As expected, this vertex diverges at a valley polarization instability, where $(2V_0' - V_0)\Pi = -1$, but remains positive, i.e., repulsive.

At a finite field, the analysis of the pairing vertex is again more involved as the condition for the valley polarization instability does not decouple between fermions with spin up and down. Performing the calculations, we find that

$$\Gamma_{\uparrow,\uparrow} = V_0' \frac{(1 + V_0 \Pi_\downarrow)^2}{Z}, \quad \Gamma_{\downarrow,\downarrow} = V_0' \frac{(1 + V_0 \Pi_\uparrow)^2}{Z}, \quad (29)$$

where

$$Z = \left(1 - V_0^2 \Pi_\downarrow \Pi_\uparrow\right)^2 - (V_0')^2(\Pi_\downarrow + \Pi_\uparrow + 2V_0 \Pi_\downarrow \Pi_\uparrow)^2. \quad (30)$$

Both $\Gamma_{\uparrow,\uparrow}$ and $\Gamma_{\downarrow,\downarrow}$ are repulsive and diverge at the valley instability at a finite $B_\parallel$, Eq. (27), as we can straightforwardly verify. Still, for $|\Pi_\uparrow| > |\Pi_\downarrow|$, $\Gamma_{\downarrow,\downarrow}$ is reduced at intermediate frequencies because of the factor $(1 + V_0 \Pi_\uparrow)^2$ in the numerator. It then still remains nonmonotonic, at least at small $V_0'/V_0 - 1$, and allows a superconducting solution with a sign-changing gap.

## VII. VALLEY-TRIPLET $p$-WAVE PAIRING

The nominally repulsive valley-preserving interaction $V_0$ in Eq. (1) also gives rise to an attraction at a finite $B$ in another spin-triplet channel, this time valley triplet and spatially odd.

The mechanism here is the field-induced KL effect in 2D – the development of an attractive $p$-wave component of the static pairing interaction due to screening by particle-hole polarization bubbles. This effect has been analyzed in Refs. [61,62]. Here we apply it to BBG.

To understand the field-induced KL effect, assume phenomenologically that the static pairing interaction $\Gamma_{ss}(0, q)$ remains proportional to valley polarization susceptibility $\chi_{v,s}$ from Eq. (5) for all $q < 2k_F$, relevant to superconductivity, and compute the polarization $\Pi_{0,s}$ explicitly. Let's do this first for a parabolic $\epsilon_i(p)$ near $K$ and $K'$. The result is well known: in 2D, $\Pi_s(0, q) = -(m/2\pi)$ for $q < 2k_{F,s}$ and $-(m/2\pi)(1 - \sqrt{4k_{F,s}^2/q^2})$ for $q > 2k_{F,s}$. At $B = 0$, $k_{F,s} = k_F$ is the same for up- and down-spins. In this situation, $\Pi_s(0, q) = -m/(2\pi)$ is $q$-independent for relevant $q < 2K_F$, and the effective interaction $\Gamma_{ss}(0, q)$ has only an $s$-wave repulsive component, like the bare $V_0$. This is commonly known as the absence of KL effect in 2D for a parabolic dispersion [63]. The situation changes at a finite $B$. Now the effective interaction between majority-spin fermions comes from the minority-spin fermions and vice versa. Because the Fermi momentum $k_{F,\uparrow}$ is larger than $k_{F,\downarrow}$, there is a range $2k_{F,\downarrow} < q < 2k_{F,\uparrow}$, where the interaction $\Gamma_{\uparrow\uparrow}(0, q)$ for spin-up fermions at momentum transfer on their Fermi surface, $q < 2k_{F,\uparrow}$ acquires a momentum dependence via the momentum dependence of $\Pi_\downarrow(0, q)$. There is no such effect for $\Gamma_{\downarrow\downarrow}(0, q)$ at $q < 2k_{F,\downarrow}$.

Once $\Gamma_{\uparrow\uparrow}(0, q)$ becomes momentum-dependent, one can search for spatially-odd solutions $\Delta(\theta)$, subject to $\int d\theta \Delta(\theta) = 0$ and $\Delta(\theta + \pi) = -\Delta(\theta)$, where $\theta$ is an angle along the Fermi surface measured from, e.g., the $k_x$ direction. These gap functions are necessarily valley triplets. The analysis of the pairing instability is rather standard, and we just present the result. We find that the $q$ dependence of the interaction gives rise to an attraction for spatially odd $\Delta(\theta)$. At a small $B_\parallel$ field, the gap equation is approximately local in $\theta$ and the $p$-wave transition temperature is $T_c \sim E_F e^{-1/\lambda_{KL}}$, where

$$\lambda_{KL} = \frac{mV_0}{8\pi^2 \delta^2} \frac{\mu_B B}{E_F}. \tag{31}$$

At small $B$, $T_c$ increases exponentially with the field. At a larger $B$, the prefactor gets smaller as the number of minority-spin fermions decreases. As a result, $T_c$ has a dome-like shape as a function of $B$. We also note that Eq. (31) is valid when $\lambda_{KL} < 1$. At larger $\lambda_{KL}$, the coupling gets renormalized by the fermionic self-energy and eventually saturates. The analysis can be straightforwardly extended to the physically relevant case when the instability first develops for spin-up fermions, i.e., when $\Gamma_{\uparrow\uparrow}(0, 0) \propto 1/\delta_\uparrow$ is much larger than $\Gamma_{\downarrow\downarrow}(0, 0) \propto 1/\delta_\downarrow$. One can model this by nonequal DOS for up and down spins. We found that Eq. (31) holds, but $\delta^2$ in Eq. (31) has to be replaced by $\delta_\downarrow^2$. One can also move away from parabolic dispersion and include the $q$ dependence of $\Pi(0, q)$ at $q < 2k_F$. This will (i) reduce $T_c$ and (ii) set a finite threshold on a $B_\parallel$ field as a field-induced attraction has to compete with a repulsive bare interaction in the valley-triplet channel which is activated by the $q$ dependence of $\Pi(0, q)$. As a result, $T_c$ as a function of $B_\parallel$ displays a dome-like behavior above a finite threshold, much like for valley-singlet $s$-wave pairing. We
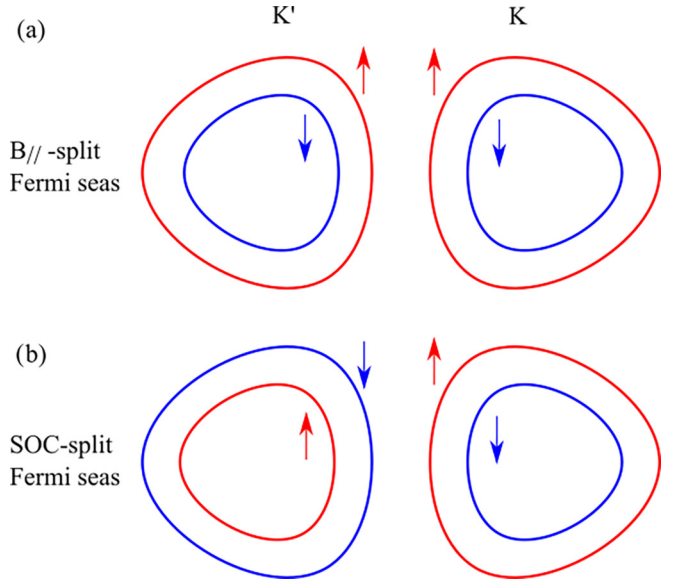


FIG. 8. Fermi seas in valleys $K$ and $K'$ split by (a) Zeeman interaction with an external field $B_\parallel$ and (b) by a spin-orbit coupling. Red (blue) arrows represent spin polarization.

believe that both pairing mechanisms, the $s$-wave discussed above and the $p$-wave discussed in this section, are possible in BBG, though the $s$-wave superconductivity is more likely to occur. This is because $s$-wave superconductivity does not rely on the Fermi surface shape, while our $p$-wave mechanism requires the Fermi surface to be nearly circular.

## VIII. GENERALIZATION TO SYSTEMS WITH SPIN-ORBIT INTERACTION

We argue below that the $s$-wave pairing mechanism also holds in systems with spin-orbit coupling (SOC). Indeed, the SOC interaction is similar in form to the Zeeman interaction with an in-plane magnetic field. Therefore the pairing scenario in the case of SOC is linked to the one described in previous sections by interchanging the isospins. For definiteness, we consider the valley-singlet $s$-wave pairing. We model SOC by adding to Eq. (1) an Ising SOC:

$$H_{so} = -\lambda_{so}(\psi_{K\alpha}^\dagger \sigma_{z,\alpha\beta} \psi_{K\beta} - \psi_{K'\alpha}^\dagger \sigma_{z,\alpha\beta} \psi_{K'\beta}). \tag{32}$$

This term plays a role of a valley-dependent effective Zeeman field $B_{so,\tau}$, ($\tau = K, K'$) that is directed transversely to the plane and has opposite signs for opposite valleys: $B_{so,K} = \frac{\lambda_{so}}{\mu_B}z$, and $B_{so,K'} = -\frac{\lambda_{so}}{\mu_B}z$, where $z$ is the unit vector perpendicular to the graphene plane. As a result, the four-fold degeneracy of Fermi pockets is lifted to two sets of twofold degenerate pockets larger ones $K\uparrow$ and $K'\downarrow$ and smaller ones $K\downarrow$ and $K'\uparrow$, see Fig. 8.

Based on this observation, it is straightforward to map the scenario, described in Sec. V, to the case of SOC—one only needs to interchange $K'\uparrow$ and $K'\downarrow$. Like there, we find that the electrons from smaller Fermi pockets $K\downarrow$ and $K'\uparrow$, experience the same nonmonotonic pairing interaction as in Eq. (14), which gives rise to an s-wave valley-singlet/spin-triplet superconductivity. It is essential that the superconducting order is still robust against an in-plane magnetic field $B_\parallel x$ and exceeds

the Pauli limit [here $\boldsymbol{x}$ is a unit vector parallel to the graphene plane]. This is so because the total effective Zeeman fields in valleys $\boldsymbol{K}$ and $\boldsymbol{K}'$

$$\boldsymbol{B_K} = \frac{\lambda_{so}}{\mu_B}z + B_\parallel \boldsymbol{x}, \quad \boldsymbol{B_{K'}} = -\frac{\lambda_{so}}{\mu_B}z + B_\parallel \boldsymbol{x}, \quad (33)$$

have the same magnitudes in the presence of both $B_\parallel$ and $\lambda_{so}$, so the Fermi surface degeneracy holds. The fact that $\boldsymbol{B}_{eff,K}$ and $\boldsymbol{B}_{eff,K'}$ are no longer parallel or anti-parallel does not matter as there is no exchange interactions between the electrons near $\boldsymbol{K}$ and $\boldsymbol{K}'$. Similarly, the analysis of valley-triplet $p$-wave pairing in the presence of SOC is parallel to that in Sec. VII.

## IX. RELATION TO EXPERIMENTS

We now discuss several points related to experiments. We will use existing measurements to justify our underlying assumptions and describe how our SC scenario can be tested experimentally. First, in our analysis of valley-singlet SC we assumed that isospin order sets in first for the majority-spin fermions. To verify that this interpretation of the phase transition is correct, below we calculate the slope of the phase boundary and compare it with the experiment. According to our model, instability happens only in the majority spin. Therefore, at the phase transition, the density of carriers in the majority spin is a fixed value, while the density of carriers in the minority spin depends on the $B_\parallel$ field. Specifically, we expect that the phase transition shifts towards lower total carrier density under increasing $B_\parallel$. The shift of carrier density is linear in the $B_\parallel$ field:

$$\frac{dn_*}{dB} = 2\mu_B \nu_0, \quad (34)$$

where $n_*$ is the total carrier density at the phase boundary, $\mu_B$ is the Bohr magneton, $\nu_0$ is the density of states per isospin, the factor of 2 arises from $\boldsymbol{K}/\boldsymbol{K}'$ valley degeneracy. Plugging in the value of the density of states obtained numerically in Ref. [20], we find the slope is $\frac{dn_*}{dB} = 5 \times 10^{-4} \, \text{nm}^{-2}\,\text{meV}^{-1}$, which matches the slope extracted from Fig. 1(c).

Second, as discussed above, the two scenarios for field-induced SC both yield dome-shaped $T_c$ as a function of carrier density, with a threshold on $B_\parallel$. The only difference between the two scenarios is which spin components pair: valley-singlet pairing involves minority spins, whereas valley-triplet pairing involves majority spins. One way to test which spin components are involved in SC is to measure the DC voltage drop when injecting a spin-polarized current into the system. For instance, we can inject electrons from a ferromagnetic material that is polarized by the same in-plane magnetic field as in the BBG, then our theory predicts that for valley-singlet pairing, this spin-polarized current should give a finite DC voltage drop even when the temperature is below $T_c$ because the SC only occurs in the Fermi sea of minority-spin electrons, while for valley-triplet pairing a DC voltage drop should disappear below $T_c$.

Third, valley-singlet pairing arises from small-momentum (forward) scattering and thus should be sensitive to screening. Accordingly, we expect this SC to become suppressed when a proximal metal gate is introduced to screen the Coulomb interaction. On the contrary, for valley-triplet pairing, SC becomes

strengthened by a proximal gate since the small-momentum scattering is harmful to this pairing channel and is strongly screened, whereas the large-momentum (backward) scattering that helps the pairing is not so strongly screened.

Fourth, we argued that SOC plays the same role as a magnetic field and gives rise to valley-singlet $s$-wave or valley-triplet $p$-wave pairing. A recent experiment [21] found SC in a BBG on a monolayer of tungsten diselenide (WSe$_2$), a source of interfacial SOC in graphene. The observed SC develops already at zero fields and exceeds the Pauli limit in the presence of a parallel field. This fully agrees with our theory.

Finally, one might ask whether the quantum-critical mode will contribute to resistivity through carrier scattering by thermal fluctuations. While this may seem plausible at first glance, we note that the effective interaction mediated by a soft boson is strong only for small momentum transfers $q \ll k_F$. This translates into near-forward scattering processes that do not produce a current relaxation and thus do not contribute to resistivity [64]. These expectations are in line with a recent experiment [20] where resistivity $T$ dependence shows no sign of critical fluctuations near the phase transition.

We are therefore led to conclude that all the unique aspects of the observed superconductivity are successfully explained by the attraction-from-repulsion-based pairing scenario. Furthermore, this mechanism is "natural" as it arises from the strong electron-electron interactions that drive the adjacent isospin-polarized electron orders. As such, it constitutes a unique, verifiable instance of an exotic pairing. Supported by experiments, it sheds light on the origin of spin-triplet superconductivity in BBG and is applicable to a variety of other systems of interest.

## APPENDIX: SELF-ENERGY AND SUPERCONDUCTIVITY

In this section, we elaborate on the effect of self-energy correction and show that it has a marginal impact on superconductivity. Here, we focus on the case of $\nu_1 = 0$. The self-energy for spin-down electrons is given by

$$\begin{aligned}
\Sigma_{\downarrow\downarrow}(\omega) &= \int \frac{d\nu}{2\pi} \int \frac{dq_\perp}{2\pi} \frac{\overline{\Gamma}_{\downarrow\downarrow}(\nu, q)}{i(\omega + \nu) - v_F q_\perp} \\
&= \frac{\lambda}{2} \int \frac{d\nu}{2\pi} \text{sgn}(\nu + \omega) S(\nu/\nu_0) \\
&= \lambda \nu_0 \int_0^{\bar{\omega}} dx\, S(x). \quad (A1)
\end{aligned}$$

To see the relevant scale of $\omega$ in the pairing problem, we look at the gap equation without self-energy correction Eq. (23). We rewrite it as follows:

$$\Delta(n) = -\frac{\lambda}{2} \sum_{n'} \frac{\Delta(n')}{|2n'+1|} S(2\pi \bar{T}_c(n-n'), 0), \quad \text{(A2)}$$

where we have rewritten $\bar{\omega} = \pi(2n+1)\bar{T}_c$, $\bar{\omega}' = \pi(2n'+1)\bar{T}_c$. As shown by numerics in the main text, the critical temperature is $T_c \sim \frac{1}{2}\lambda\nu_0 \times 10^{-2}$. For extremely large value of $\lambda \gg 10^2$ (i.e., extremely small $\delta_\downarrow$), the relevant $n, n' \sim O(1)$. Replacing $S(x)$ with its asymptotic form $\frac{1}{2x}$, we find numerically that the wavefunction stop changing sign at $n = 4$. The self-energy relevant for this pairing problem should be evaluated at $\omega = 9\pi T_c$:

$$\Sigma_{\downarrow\downarrow}(\omega \sim 9\pi T_c) \sim \lambda\nu_0 \ln(\lambda), \quad \text{(A3)}$$

where logarithm comes from integrating $S(x)$ which scales as $\frac{1}{2x}$ at large $x$. Then, we find the effective coupling scales with $\lambda$ as

$$\tilde{\lambda} = \frac{\lambda}{1 + \kappa \ln \lambda}, \quad \kappa \sim \frac{100}{9\pi} = 3.5. \quad \text{(A4)}$$

The denominator is only marginally relevant at large $\lambda$, thus does not suppress the $T_c$ substantially.

For a not-so-large $\lambda$ value ($\lambda < 10^2$), the relevant value of $n, n'$ the equation above is $n, n' \lesssim \nu_0/T_c = 10^2/\lambda$. The self-energy relevant for this pairing problem should be evaluated at $\omega \lesssim \nu_0$:

$$\Sigma_{\downarrow\downarrow}(\omega \sim \nu_0) \sim 0.2\lambda\nu_0, \quad \text{(A5)}$$

where the numerical factor comes from integrating $S(x)$ below the turning pint $x \sim 0.5$. We find the effective coupling scales with $\lambda$ as

$$\tilde{\lambda} = \frac{\lambda}{1 + 0.2\lambda}. \quad \text{(A6)}$$

In this case, carrying out the simulation as in the main text (see Fig. 7 and accompanying discussion), we get $T_c \sim 10^{-4}E_F$. This value is much smaller than the ones in Fig. 7 but still of an acceptable order of magnitude.

[1] Y. Cao, V. Fatemi, S. Fang, K. Watanabe, T. Taniguchi, E. Kaxiras, and P. Jarillo-Herrero, Unconventional superconductivity in magic-angle graphene superlattices, Nature (London) **556**, 43 (2018).

[2] X. Lu, P. Stepanov, W. Yang, M. Xie, M. A. Aamir, I. Das, C. Urgell, K. Watanabe, T. Taniguchi, G. Zhang, A. Bachtold, A. H. MacDonald, and E. Dmitri, Superconductors, orbital magnets and correlated states in magic-angle bilayer graphene, Nature (London) **574**, 653 (2019).

[3] E. Y. Andrei and A. H. MacDonald, Graphene bilayers with a twist, Nat. Mater. **19**, 1265 (2020).

[4] Y. Saito, J. Ge, K. Watanabe, T. Taniguchi, and A. F. Young, Independent superconductors and correlated insulators in twisted bilayer graphene, Nat. Phys. **16**, 926 (2020).

[5] M. Oh, K. P. Nuckolls, D. Wong, R. L. Lee, X. Liu, K. Watanabe, T. Taniguchi, and A. Yazdani, Evidence for unconventional superconductivity in twisted bilayer graphene, Nature (London) **600**, 240 (2021).

[6] Y. Cao, D. Rodan-Legrain, J. M. Park, N. F. Q. Yuan, K. Watanabe, T. Taniguchi, R. M. Fernandes, L. Fu, and P. Jarillo-Herrero, Nematicity and competing orders in superconducting magic-angle graphene, Science **372**, 264 (2021).

[7] A. Jaoui, I. Das, G. Di Battista, J. Díez-Mérida, X. Lu, K. Watanabe, T. Taniguchi, H. Ishizuka, L. Levitov, and D. K. Efetov, Quantum critical behaviour in magic-angle twisted bilayer graphene, Nat. Phys. **18**, 633 (2022).

[8] R. Bistritzer and A. H. MacDonald, Moiré bands in twisted double-layer graphene, Proc. Natl. Acad. Sci. USA **108**, 12233 (2011).

[9] L. Balents, C. R. Dean, D. K. Efetov, and A. F. Young, Superconductivity and strong correlations in moiré flat bands, Nat. Phys. **16**, 725 (2020).

[10] X. Liu, Z. Wang, K. Watanabe, T. Taniguchi, O. Vafek, and J. Li, Tuning electron correlation in magic-angle twisted bilayer graphene using coulomb screening, Science **371**, 1261 (2021).

[11] Y.-Z. You and A. Vishwanath, Superconductivity from valley fluctuations and approximate SO(4) symmetry in a weak coupling theory of twisted bilayer graphene, npj Quantum Mater. **4**, 16 (2019).

[12] V. Kozii, H. Isobe, J. W. F. Venderbos, and L. Fu, Nematic superconductivity stabilized by density wave fluctuations: Possible application to twisted bilayer graphene, Phys. Rev. B **99**, 144507 (2019).

[13] D. V. Chichinadze, L. Classen, and A. V. Chubukov, Nematic superconductivity in twisted bilayer graphene, Phys. Rev. B **101**, 224513 (2020).

[14] E. Khalaf, S. Chatterjee, N. Bultinck, M. P. Zaletel, and A. Vishwanath, Charged skyrmions and topological origin of superconductivity in magic-angle graphene, Sci. Adv. **7**, eabf5299 (2021).

[15] P. Stepanov, I. Das, X. Lu, A. Fahimniya, K. Watanabe, T. Taniguchi, F. H. Koppens, J. Lischner, L. Levitov, and D. K. Efetov, Untying the insulating and superconducting orders in magic-angle graphene, Nature (London) **583**, 375 (2020).

[16] F. Wu, A. H. MacDonald, and I. Martin, Theory of Phonon-Mediated Superconductivity in Twisted Bilayer Graphene, Phys. Rev. Lett. **121**, 257001 (2018).

[17] B. Lian, Z. Wang, and B. A. Bernevig, Twisted Bilayer Graphene: A Phonon-Driven Superconductor, Phys. Rev. Lett. **122**, 257002 (2019).

[18] F. Wu, E. Hwang, and S. Das Sarma, Phonon-induced giant linear-in-$T$ resistivity in magic angle twisted bilayer graphene: Ordinary strangeness and exotic superconductivity, Phys. Rev. B **99**, 165112 (2019).

[19] G. Tarnopolsky, A. J. Kruchkov, and A. Vishwanath, Origin of Magic Angles in Twisted Bilayer Graphene, Phys. Rev. Lett. **122**, 106405 (2019).

[20] H. Zhou, L. Holleis, Y. Saito, L. Cohen, W. Huynh, C. L. Patterson, F. Yang, T. Taniguchi, K. Watanabe, and A. F. Young, Isospin magnetism and spin-polarized superconductivity in bernal bilayer graphene, Science **375**, 774 (2022).

[21] Y. Zhang, R. Polski, A. Thomson, É. Lantagne-Hurtubise, C. Lewandowski, H. Zhou, K. Watanabe, T. Taniguchi, J. Alicea, and S. Nadj-Perge, Enhanced superconductivity in spin-orbit proximitized bilayer graphene, Nature (London) **613**, 268 (2023).

[22] H. Zhou, T. Xie, A. Ghazaryan, T. Holder, J. R. Ehrets, E. M. Spanton, T. Taniguchi, K. Watanabe, E. Berg, M. Serbyn *et al.*, Half- and quarter-metals in rhombohedral trilayer graphene, Nature (London) **598**, 429 (2021).

[23] H. Zhou, T. Xie, T. Taniguchi, K. Watanabe, and A. F. Young, Superconductivity in rhombohedral trilayer graphene, Nature (London) **598**, 434 (2021).

[24] A. Klein, A. V. Chubukov, Y. Schattner, and E. Berg, Normal State Properties of Quantum Critical Metals at Finite Temperature, Phys. Rev. X **10**, 031053 (2020).

[25] V. Oganesyan, S. A. Kivelson, and E. Fradkin, Quantum theory of a nematic fermi fluid, Phys. Rev. B **64**, 195109 (2001).

[26] S. Lederer, Y. Schattner, E. Berg, and S. A. Kivelson, Enhancement of Superconductivity near a Nematic Quantum Critical Point, Phys. Rev. Lett. **114**, 097001 (2015).

[27] A.-M. S. Tremblay, Strongly correlated superconductivity, in *Autumn School on Correlated Electrons: Emergent Phenomena in Correlated Matter*, edited by E. Pavarini, E. Koch, and U. Schollwöck (Forschungszentrum Jülich, Germany, 2013).

[28] A. V. Chubukov, A. Abanov, Y. Wang, and Y.-M. Wu, The interplay between superconductivity and non-fermi liquid at a quantum-critical point in a metal, Ann. Phys. **417**, 168142 (2020).

[29] E. Berg, S. Lederer, Y. Schattner, and S. Trebst, Monte carlo studies of quantum critical metals, Annu. Rev. Condens. Matter Phys. **10**, 63 (2019).

[30] S.-S. Lee, Recent developments in non-fermi liquid theory, Annu. Rev. Condens. Matter Phys. **9**, 227 (2018).

[31] K. B. Efetov, H. Meier, and C. Pepin, Pseudogap state from quantum criticality, Nat. Phys. **9**, 442 (2013).

[32] P. Monthoux, D. Pines, and G. G. Lonzarich, Superconductivity without phonons, Nature (London) **450**, 1177 (2007).

[33] I. I. Mazin, D. J. Singh, M. D. Johannes, and M. H. Du, Unconventional Superconductivity with a Sign Reversal in the Order Parameter of LaFeAsO$_{1-x}$F$_x$, Phys. Rev. Lett. **101**, 057003 (2008).

[34] I. Mazin and J. Schmalian, Pairing symmetry and pairing state in ferropnictides: Theoretical overview, Physica C: Superconductivity **469**, 614 (2009).

[35] A. Abanov, A. V. Chubukov, and J. Schmalian, Quantum-critical theory of the spin-fermion model and its application to cuprates: Normal state analysis, Adv. Phys. **52**, 119 (2003).

[36] W. Qin, C. Huang, T. Wolf, N. Wei, I. Blinov, and A. H. MacDonald, Functional Renormalization Group Study of Superconductivity in Rhombohedral Trilayer Graphene, Phys. Rev. Lett. **130**, 146001 (2023).

[37] A. Ghazaryan, T. Holder, M. Serbyn, and E. Berg, Unconventional Superconductivity in Systems with Annular Fermi Surfaces: Application to Rhombohedral Trilayer Graphene, Phys. Rev. Lett. **127**, 247001 (2021).

[38] Y.-Z. Chou, F. Wu, J. D. Sau, and S. Das Sarma, Acoustic-phonon-mediated superconductivity in bernal bilayer graphene, Phys. Rev. B **105**, L100503 (2022).

[39] P. Morel and P. W. Anderson, Calculation of the superconducting state parameters with retarded electron-phonon interaction, Phys. Rev. **125**, 1263 (1962).

[40] W. L. McMillan, Transition temperature of strong-coupled superconductors, Phys. Rev. **167**, 331 (1968).

[41] N. N. Bogoljubov, V. V. Tolmachov, and D. V. Širkov, A new method in the theory of superconductivity, Fortschr. Phys. **6**, 605 (1958).

[42] P. Coleman, *Introduction to Many-Body Physics* (Cambridge University Press, Cambridge, 2015).

[43] J. Ruhman and P. A. Lee, Superconductivity at very low density: The case of strontium titanate, Phys. Rev. B **94**, 224515 (2016).

[44] A. Chubukov, N. V. Prokof'ev, and B. V. Svistunov, Implicit renormalization approach to the problem of Cooper instability, Phys. Rev. B **100**, 064513 (2019).

[45] D. Pimenov and A. V. Chubukov, Quantum phase transition in a clean superconductor with repulsive dynamical interaction, npj Quantum Mater. 7, 45 (2022).

[46] W. Kohn and J. M. Luttinger, New Mechanism for Superconductivity, Phys. Rev. Lett. **15**, 524 (1965).

[47] S. Chatterjee, T. Wang, E. Berg, and M. P. Zaletel, Inter-valley coherent order and isospin fluctuation mediated superconductivity in rhombohedral trilayer graphene, Nat. Commun. **13**, 6013 (2022).

[48] Z. Dong, P. A. Lee, and L. S. Levitov, Signatures of Cooper pair dynamics and quantum-critical superconductivity in tunable carrier bands, arXiv:2304.09812.

[49] J. Jung, F. Zhang, and A. H. MacDonald, Lattice theory of pseudospin ferromagnetism in bilayer graphene: Competing interaction-induced quantum hall states, Phys. Rev. B **83**, 115408 (2011).

[50] E. McCann and M. Koshino, The electronic properties of bilayer graphene, Rep. Prog. Phys. **76**, 056503 (2013).

[51] Z. Dong, M. Davydova, O. Ogunnaike, and L. Levitov, Isospin- and momentum-polarized orders in bilayer graphene, Phys. Rev. B **107**, 075108 (2023).

[52] Z. Dong and L. Levitov, Superconductivity in the vicinity of an isospin-polarized state in a cubic Dirac band, arXiv:2109.01133.

[53] D. V. Chichinadze, L. Classen, Y. Wang, and A. V. Chubukov, SU(4) Symmetry in Twisted Bilayer Graphene: An Itinerant Perspective, Phys. Rev. Lett. **128**, 227601 (2022).

[54] A. V. Chubukov and P. Wölfle, Quasiparticle interaction function in a two-dimensional fermi liquid near an antiferromagnetic critical point, Phys. Rev. B **89**, 045108 (2014).

[55] D. Chowdhury, A. Georges, O. Parcollet, and S. Sachdev, Sachdev-ye-kitaev models and beyond: Window into non-fermi liquids, Rev. Mod. Phys. **94**, 035004 (2022).

[56] P. A. Lee, Gauge Field, Aharonov-Bohm Flux, and High-$T_c$ Superconductivity, Phys. Rev. Lett. **63**, 680 (1989).

[57] B. Blok and H. Monien, Gauge theories of high-$T_c$ superconductors, Phys. Rev. B **47**, 3454 (1993).

[58] C. Nayak and F. Wilczek, Non-fermi liquid fixed point in 2 + 1 dimensions, Nucl. Phys. B **417**, 359 (1994).

[59] B. L. Altshuler, L. B. Ioffe, and A. J. Millis, Low-energy properties of fermions with singular interactions, Phys. Rev. B **50**, 14048 (1994).

[60] Y. B. Kim, A. Furusaki, X.-G. Wen, and P. A. Lee, Gauge-invariant response functions of fermions coupled to a gauge field, Phys. Rev. B **50**, 17917 (1994).

[61] M. Y. Kagan and A. V. Chubukov, Increase in superfluid transition temperature in polarized Fermi gas with repulsion, Sov. JETP Lett. **50**, 517 (1989).

[62] S. Raghu and S. A. Kivelson, Superconductivity from repulsive interactions in the two-dimensional electron gas, Phys. Rev. B **83**, 094518 (2011).

[63] M. A. Baranov and M. Y. Kagan, Superconductivity in a low-density two-band model with a repulsive interaction: Extended analysis, J. Exp. Theor. Phys. **75**, 165 (1992).

[64] D. L. Maslov, V. I. Yudson, and A. V. Chubukov, Resistivity of a Non-Galilean–Invariant Fermi Liquid near Pomeranchuk Quantum Criticality, Phys. Rev. Lett. **106**, 106403 (2011).